Journal of Ceramic Processing Research. Vol. 26, No. 3, pp. 397~405 (2025)
(Received 20 December 2024, Received in revised form 4 March 2025, Accepted 14 April 2025)
https://doi.org/10.36410/jcpr.2025.26.3.397

J O U R N A L O F
Ceramic Processing Research

Effect of lithium slag on the performance of cement mortar

Yuhan Tang[a], Youshuai Zhao[a], Xuetao Yue[a,*], Xuelei An[b], Xiaopeng Shang[c] and Chonghao Liu[d]
[a]*School of Material Science and Engineering, Shandong Jianzhu University, Jinan 250101, China*
[b]*Shandong Survey and Design Institute of Water Conservancy Co.,Ltd, Jinan 250013, China*
[c]*Shandong Urban Construction Vocational College, Jinan 250103, China*
[d]*Jinan Energy Engineering Group Co., Ltd, Jinan 250101, China*

Lithium slag-cement composite mortar (LSCCM) was prepared by replacing part of 42.5 Ordinary Portland cement with lithium slag (LS). The effects of LS on the properties of cement mortar and its mechanism of action were analyzed by X-ray diffraction (XRD), fourier transform infrared spectroscopy (FTIR), scanning electron microscopy (SEM), heat of hydration method, nuclear magnetic resonance (NMR) technique and mercury intrusion porosity (MIP). The results showed that LS replacing part of the cement would reduce the fluidity of the system, shorten the setting time, lower the strength in the preperiod, increase the strength in the postperiod, change the pore size distribution, and would not cause changes in the hydration products. In the early stage, LS just plays a filling role, the hydration reaction rate of the LSCCM decreases, and the pores in the system become larger, resulting in a lower compressive strength than the cement mortar at 3d and 7d. In the later stage, the LS undergoes pozzolanic reaction, which makes the LSCCM become denser, and when the replacement amount of lithium slag is 20% of the cement mass, the 28d compressive strength of the LSCCM can reach 50.2 MPa, which is 9.4% higher than that of the cement mortar specimen.

Keywords: Lithium slag, Alkali-silica reaction, Mechanical properties, Porosity, Microstructure.

Introduction

With the development of the new energy vehicle industry, various types of batteries have become the main object of research for various companies. Although there are different types of batteries on the market, lithium batteries are still the most widely used [1-3]. Currently, lithium and some of its compounds are mainly extracted from lithium pyroxene ore, and partly from lithium mica [4]. However, every 1 ton of lithium carbonate production will produce more than 8 tons of LS [5-8]. The traditional treatment of LS is to place it in natural piles Natural piles take up a lot of land, and the substances carried away by rainwater will cause great damage to the local ecological environment, and irrational storage is bound to pollute the environment [9, 10]. Therefore, the utilization of LS is of great significance to sustainable development and has great environmental and economic benefits.

It has been reported that LS can partially replace clay in the production of cement clinker, but the high SO_3 content of LS may affect the stability of cement clinker [11]. LS can also be used to prepare lightweight aggregates. Xiong et al. successfully prepared lightweight ceramic granules using LS and fly ash with an apparent density and bulk density of 0.86 and 0.46 kg/m^3, respectively, and a compressive strength of 1.76 MPa, and water absorption of 0.96% [12]. Gao et al. produced lightweight aggregates using contaminated soil and lithium slag, which had good performance with a density of 0.5-1.5 g/cm^3 and a compressive strength of 1.0-8.7 MPa [13]. Furthermore, Luo et al. suggested a one-part mixing approach for the high-volume and effective synthesis of LS geopolymer cement. The findings demonstrated that while LS reduced the hydration heat of the LS geopolymer, it had a detrimental effect on the fluidity of the geopolymer. When 50% LS was used, the geopolymer's ideal 28d compressive strength was 32.5 MPa, which may be utilized as a subpar building material in the LS production facility [14].

The main chemical composition of LS is SiO_2, Al_2O_3, which can react in the cement-LS system, called pozzolanic reaction [15]. Therefore, LS can replace part of the cement as an auxiliary cementitious material [7, 16, 17].

In this paper, lithium slag is used to replace part of the cement to prepare cementitious materials, and combined with a variety of analytical test methods, such as XRD, SEM, FT-IR, NMR, etc., to investigate the effects of the dosage of LS on the fluidity, setting time, strength, and porosity of the cement mortar. It is hoped that these results can provide a new way for the resourcing of

*Corresponding author:
Tel : +86 13589035658
Fax: +86 053186367285
E-mail: yuexuetao11@sdjzu.edu.cn

Table 1. Chemical compositions of materials in wt.%.

	CaO	SiO_2	Al_2O_3	SO_3	Fe_2O_3	MgO	Na_2O	K_2O
Cement	63.48	18.58	7.21	2.81	4.21	1.67	0.23	0.58
LS	9.12	48.26	20.19	14.04	1.38	0.81	0.29	0.57

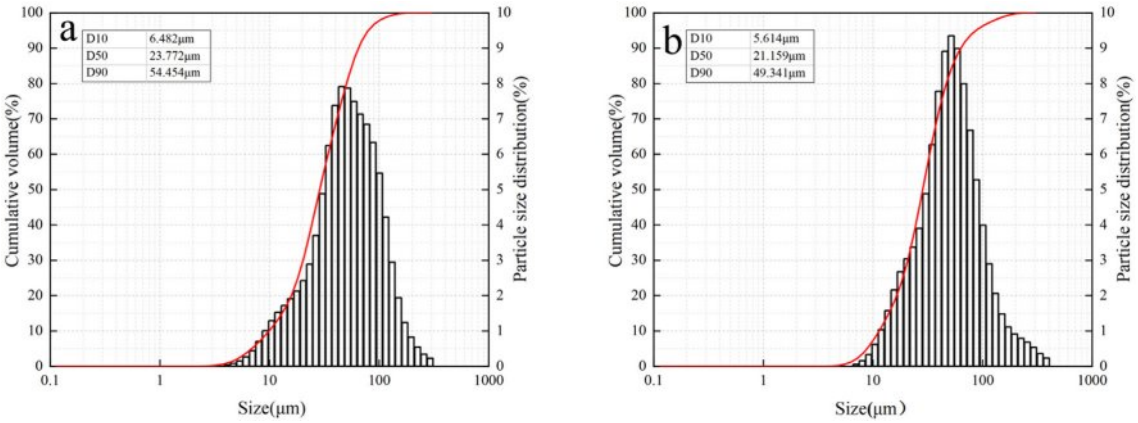

Fig. 1. Particle size distribution: (a) cement; (b) LS.

LS, as well as a reference opinion for other solid waste treatment in the field of cement and concrete.

Materials and Methods

Materials

Cement was obtained as 42.5 Ordinary Portland cement produced by Shangheshanshui Cement Co., Ltd. LS was from Shandong Ruifu Lithium Industry Co., Ltd. Prior to the experiment, the lithium slag was milled. The main compositions of the ground LS and cement are shown in Table 1, and the particle size distribution is shown in Fig. 1.

Fig. 2 shows the XRD pattern of LS. Gypsum ($CaSO_4 \cdot 2H_2O$), quartz (SiO_2), and spodumene ($LiAlSi_2O_6$) can be observed from the XRD pattern. The SEM image of LS is shown in Fig. 3, and irregularly shaped LS particles and columnar gypsum can be observed.

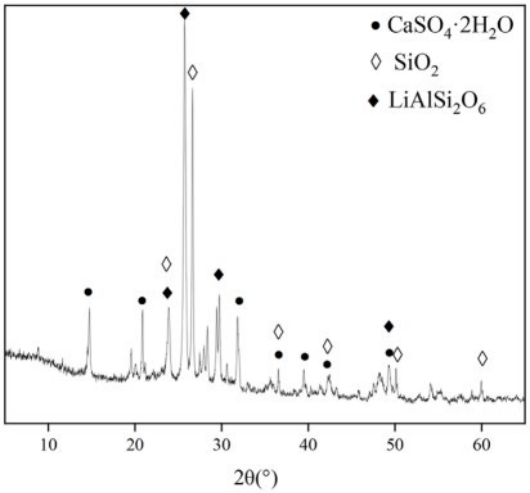

Fig. 2. XRD patterns of LS.

Sample preparation

Due to the hygroscopicity of the LS, its moisture content was 21.62%, and it was dried at 105 °C before ball milling. The LS was ground in a ball mill for 1 h. LS to stainless steel ball ratio of 1:10. Stainless steel balls with diameters of 50 mm and 25 mm were selected, with weight percentages of 70% and 30%, respectively, and the rotational speed was 200 r/min.

The specimens were prepared according to the recipe shown in Table 2, 40×40×160 mm^3 for strength tests. 24 h later, the specimens were demolded and placed in a standardized curing room (20 ± 1 °C, RH = 98 ± 2%) for testing up to the specified age.

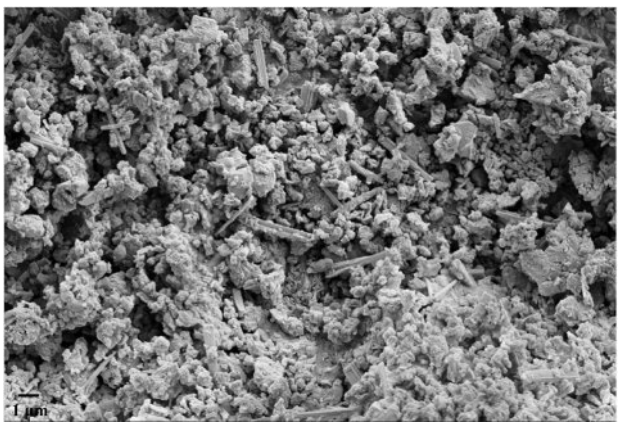

Fig. 3. SEM images of LS.

Table 2. Mix proportions of LSCCM.

Group	Mass/g				Water-binder ratio
	LS	Cement	Water	Sand	
P1	0	450	225	1350	0.5
P2	45	405			
P3	90	360			
P4	135	315			

Testing methods

Particle size distribution

The particle size distribution of the raw material was characterized using a laser particle size analyzer. Based on the Chinese national standard GB/T 2419-2005 [18] and GB/T 1346-2011 [19], the samples were tested for flowability and setting time. The samples were tested for compressive strength according to the Chinese national standard GB/T 17671-2021 [20]. The composition of the samples were analyzed using a Thermo Scientific ARL EQUINOX Pro X-ray diffractometer and a scanning range of 5°-60° (2θ). The sample powder was mixed with spectroscopically pure potassium bromide and ground and pressed, and then analyzed by a NICOLET iS5 infrared spectrometer with a wave number range of 500-4000 cm^{-1}. The heat of hydration was tested using isothermal conduction calorimetry with a CHH-CAL-8000 model instrument at a temperature of 20±1 °C. The microstructure at the fracture was characterized by SUPRA55 scanning electron microscope after spraying gold on the fracture of the samples to be tested. NMR was tested using a PQ001 LF-NMR analyzer with the intensity set at 0.3 T, and temperature at 22-28 °C. MIP was tested using an AutoPore V 9600 weighted automated mercuric piezometer, with the contact angle determined to be 130°, and the applied pressure ranging from 0.10-61000 psia.

Results and Discussion

Fluidity

Fig. 4 shows the mobility of different LSCCM samples. It can be clearly seen that as the more lithium slag replacement is increased, the fluidity of LSCCM gets worse. When the replacement amount of lithium slag is 30%, the fluidity is reduced by 8%. Numerous studies [21-25] have shown that there are two main factors affecting the rheological properties: one is the interaction between solid particles: mainly internal friction, interparticle viscous force, electric repulsion, van der Waals force, etc.; the second is the effect of hydration, with the hydration, the hydration products gradually increase, changing the shear stress and plastic viscosity of the system. In the early stage, the hydration is basically negligible, so one should not consider the effect of hydration on the fluidity; lithium slag are of irregular shape, the degree of roughness is high, which leads to an increase in friction between the particles, and therefore reduces the fluidity of the slurry. In addition, LS has a finer particle size and larger specific surface area compared to cement particles, and LS contains some gypsum, which leads to an increase in water demand, and also reduces the fluidity of LSCCM.

Setting time

Fig. 5 shows the setting time results for LS-cement paste with different lithium slag replacement. It can be seen that the setting time of the slurry is gradually shortened with the increase of LS substitution. This is mainly because the LS is relatively fine, and part contains gypsum, the water absorption is relatively strong, resulting in a large reduction in the flow of the slurry. On the other hand, the LS contains a small amount of lithium-salts [26, 27], which has a certain effect of coagulation, and has a certain effect on the

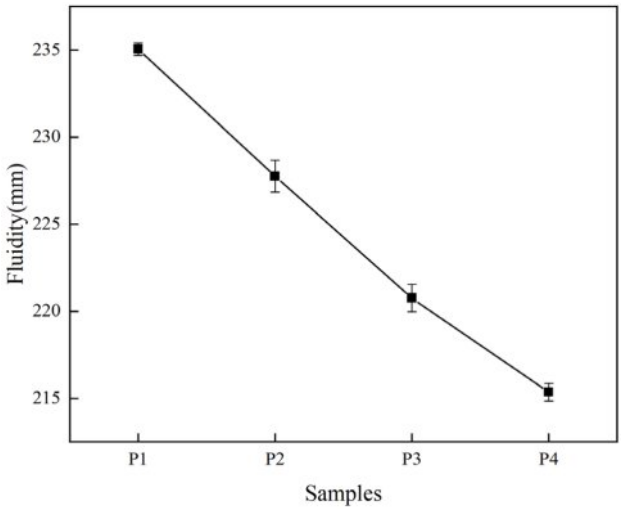

Fig. 4. Fluidity of LSCCM.

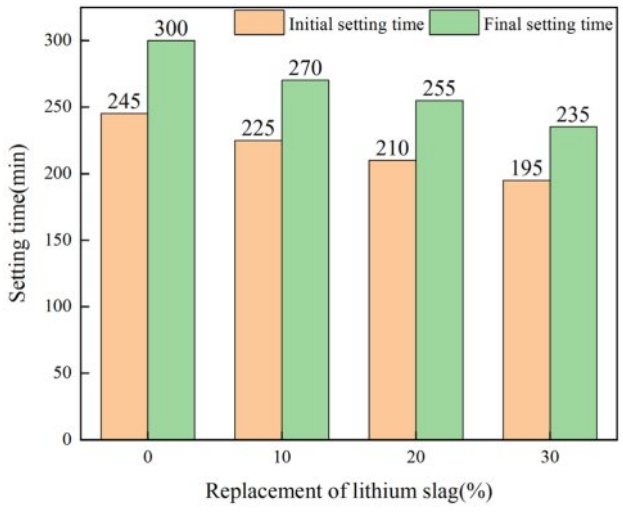

Fig. 5. Setting time of LS-cement net paste.

coagulation time. In addition, Tan et al. found that the gypsum contained in LS can accelerate the formation of ettringite (AFt), which leads to the shortening of the setting time of the LSCCM [28].

Compressive strength

The results of compressive strength of different LSCCM samples at different ages are shown in Fig. 6. At 3d and 7d, the strength of P1 group was the highest. The strength of P2-P4 groups decreased with the increase of LS substitution. This indicates that in the early stage, LS will have a negative impact on the strength of LSCCM. At 28d, the strength of samples from P2 to P3 groups are significantly higher than that of P1 group, and samples from P4 group are lower than that of P1. When LS replacement is 20%, LSCCM reaches the optimal mechanical properties, in which the compressive strength of 50.2 MPa is improved by 9.4% compared with that of P1.

In the early stage, C_3A is more susceptible to hydration reactions than C_3S, and the large amount of gypsum in LS provides SO_4^{2-} to react with C_3A to form AFt, which tends to attach to the surface of C_3S particles and hinders the hydration of C_3S to form C-S-H to provide strength. In addition, other studies [29-32] suggest that some nanoparticles can be used as nuclei for hydration reactions. However, the LS used in this paper has a D10 of 5.614 μm. therefore, it may not provide any significant level of nucleation, which mainly occurs when the cement reacts with water. In the late stage when the Ca^{2+} concentration is gradually saturated, the LS begins to exert pozzolanic reaction, and SiO_2 reacts with the hydration product $Ca(OH)_2$ to promote secondary hydration.

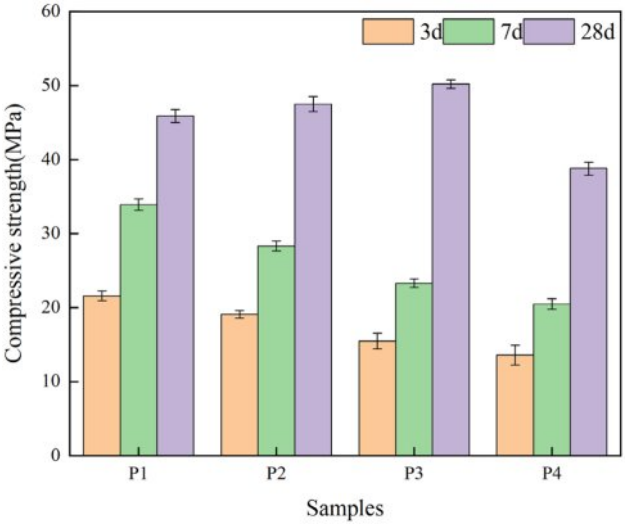

Fig. 6. Compressive strength.

XRD analysis

The XRD of LSCCM samples at different ages are shown in Fig. 7, and the hydration products of all the samples are mainly $Ca(OH)_2$ and AFt, as well as incompletely hydrated C_3S, and no new hydration products are generated. In Fig. 7(a), the intensity of the diffraction peaks of AFt increases with the increase of lithium slag repacement, and the intensity of the diffraction peaks of $Ca(OH)_2$ is opposite. This is because in the presence of gypsum, Al_2O_3 in LS and hydration to produce $Ca(OH)_2$ react to form AFt, and with the increase of lithium slag repacement, the content of C_3S hydrated to form $Ca(OH)_2$ decreases, so the intensity of $Ca(OH)_2$ diffraction peak decreases. In addition, during sample preparation, $Ca(OH)_2$ may be carbonized to produce calcite, which also affects the intensity of $Ca(OH)_2$ diffraction peaks.

In Fig. 7(b), compared with the XRD at 3 days, the hydration product types of LSCCM at 28d did not change much, but the diffraction peak intensities corresponding to $Ca(OH)_2$ and SiO_2 decreased. This is due to the pozzolanic reaction of the lithium slag as curing age increases, which promotes the hydration reaction between $Ca(OH)_2$ and SiO_2 and Al_2O_3 in the

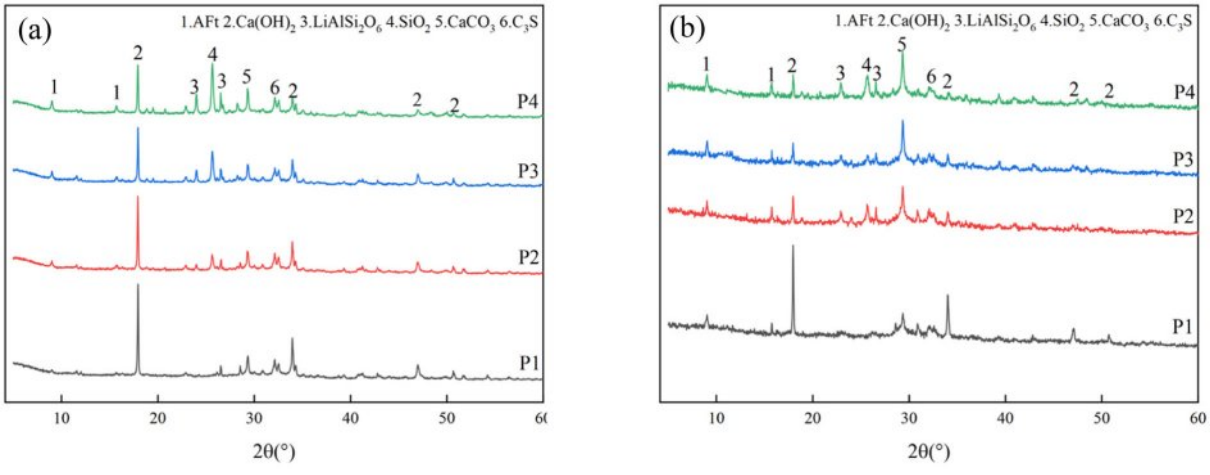

Fig. 7. XRD patterns of LSCCM: (a) 3d; (b) 28d.

LS to produce more products such as C-S-H and AFt.

FTIR analysis

The FTIR spectra of different LSCCM samples for 28 d are shown in Fig. 8. The main characteristic peaks are 3650 cm^{-1}, 3443 cm^{-1}, 1657 cm^{-1}, 1422 cm^{-1}, 1111 cm^{-1}, 984 cm^{-1}, and 875 cm^{-1}. Among them, the first peak, 3650 cm^{-1}, is the stretching vibration of the -OH of $Ca(OH)_2$ in the paste [33], and at 3443 cm^{-1} and 1657 cm^{-1}, respectively, are the H-O-H stretching vibration and H-OH bending vibration [34, 35], which may be due to the presence of adsorbed water within the pore structure as well as the presence of hydroxyl structure in the gel. 1422 cm^{-1} and 875 cm^{-1} are considered as CO_3^{2-} vibration

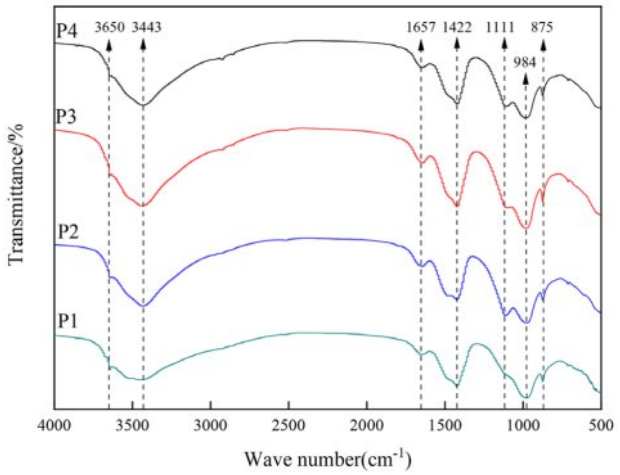

Fig. 8. FTIR spectra of LSCCM at 28 day.

[36, 37], which may be due to the calcite residue or $Ca(OH)_2$ being carbonized in the LS. The absorption peak at 1111 cm^{-1} is the asymmetric stretching vibration of SO_4^{2-}. The absorption peak at 1111 cm^{-1} is the asymmetric stretching vibration of SO_4^{2-}, and the peak here starts to become obvious with the incorporation of LS, which is attributed to the presence of part of gypsum in LS. 984 cm^{-1} out is related to the stretching vibration of the Si-O-Si group in C-S-H [28], suggesting that a gel network was formed in the LS-cement mortar.

SEM analysis

The SEM micromorphology of different LSCCM samples for 3 d is shown in Fig. 9. It can be seen that a large amount of C-S-H gel and AFt were generated inside P1. In samples P2 to P4, it can be clearly seen that some unreacted LS particles are still piled up.

The SEM micromorphology after 28d is shown in Fig. 10. Compared with Fig. 9, the hydration degree of the sample was greatly improved compared with that at 3d. A large number of C-S-H gels could be observed, and the LS particles could hardly be seen. This indicates that with the prolongation of the curing time, the cement hydration continuously produces $Ca(OH)_2$, and the alkalinity inside the system is enhanced, which promotes the decomposition of LS, and the reactive SiO_2 in LS reacts with part of the $Ca(OH)_2$ to produce C-S-H gel, which leads to a closer contact between the solid phases, and the system is more dense, thus improving the strength of LSCCM.

Heat evolution of LSCCM

The hydration heat evolution rate and cumulative

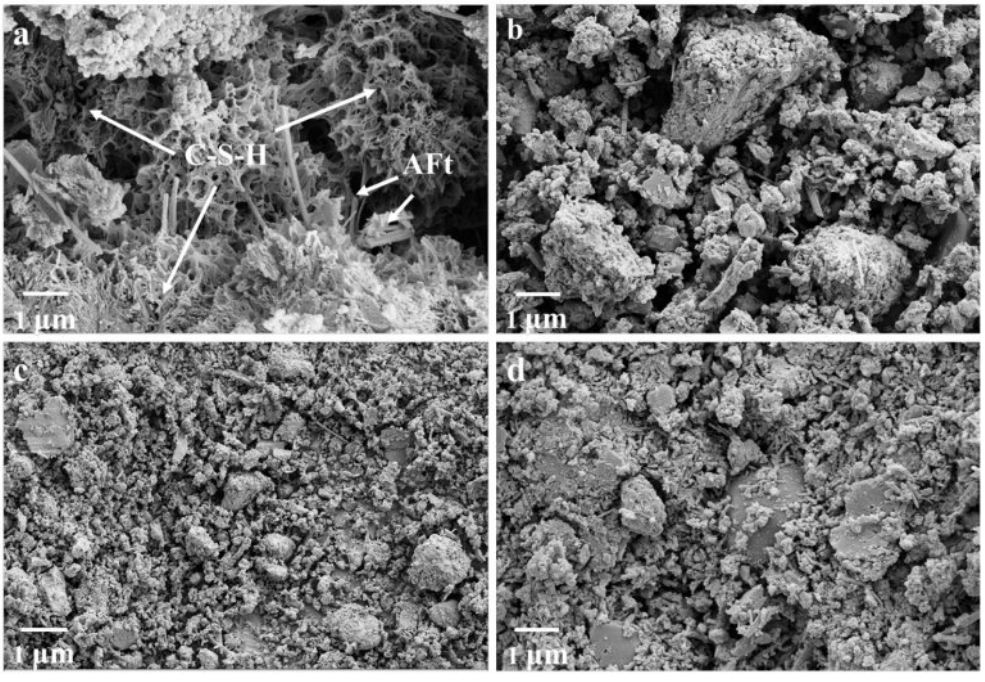

Fig. 9. SEM of hydration products of LSCCM at 3d: (a) P1; (b) P2; (c) P3; (d) P4.

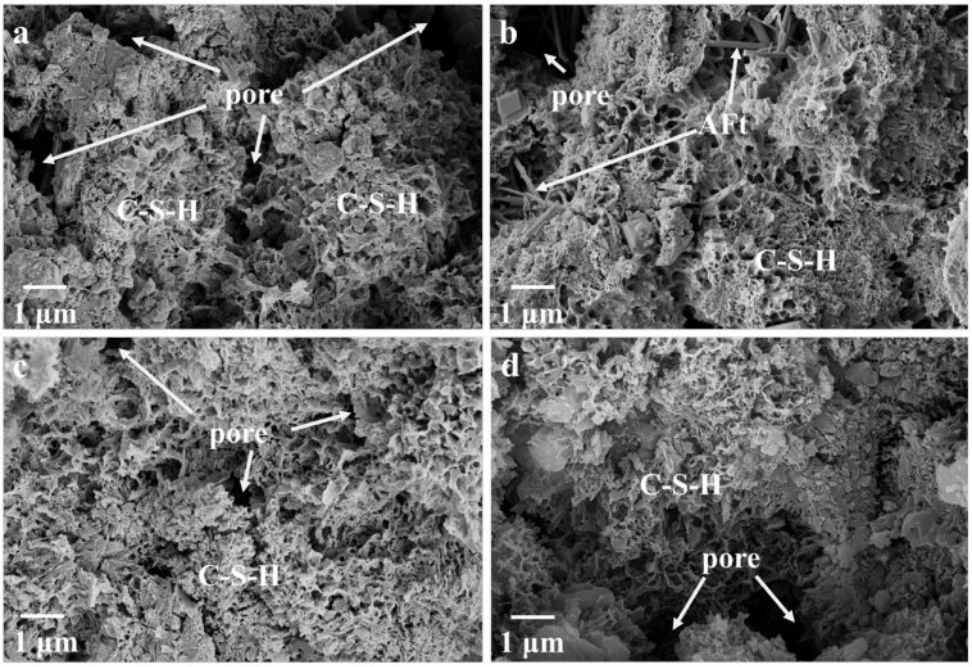

Fig. 10. SEM of hydration products of LSCCM at 28d: (a) P1; (b) P2; (c) P3; (d) P4.

exothermic heat of various LSCCM samples over a 72-hour period are displayed in Fig. 11. In accordance with the findings of earlier research, the heat of hydration can be separated into five stages, as shown in Fig. 11(a): dissolution, induction, acceleration, deceleration, and diffusion [38, 39]. In the dissolution phase of the first few minutes, a large amount of heat is released due to the rapid dissolution of silicates and aluminates in the raw material in contact with water. During the induction period, the duration of the induction period lengthens as the amount of LS replacement increases. This is due to the fact that the LS incorporation reduces the cement content, resulting in a lower Ca^{2+} concentration in the system, and hence a longer induction period. In the acceleration period, C_3S in the raw material continued to react with water to release heat energy, but due to the gradual saturation of the ionic concentration in the solution, Ca^{2+} and OH^- reacted to produce $Ca(OH)_2$ and precipitated as crystals, and C-S-H began to nucleate and grow to accelerate the hydration reaction of the cementitious material. With the increase of LS content, the exothermic peak decreases and moves to the right. This is because a higher LS replacement slows down the production time of C-S-H by lowering the amount of C_3S and C_2S in the system, which prolongs the time it takes for the ions to reach saturation. A second exothermic peak was also observed during the deceleration period, which may be due to the conversion of AFt to monosulfoaluminate (AFm) [40-43]. It is also possible that substances in the cement caused the

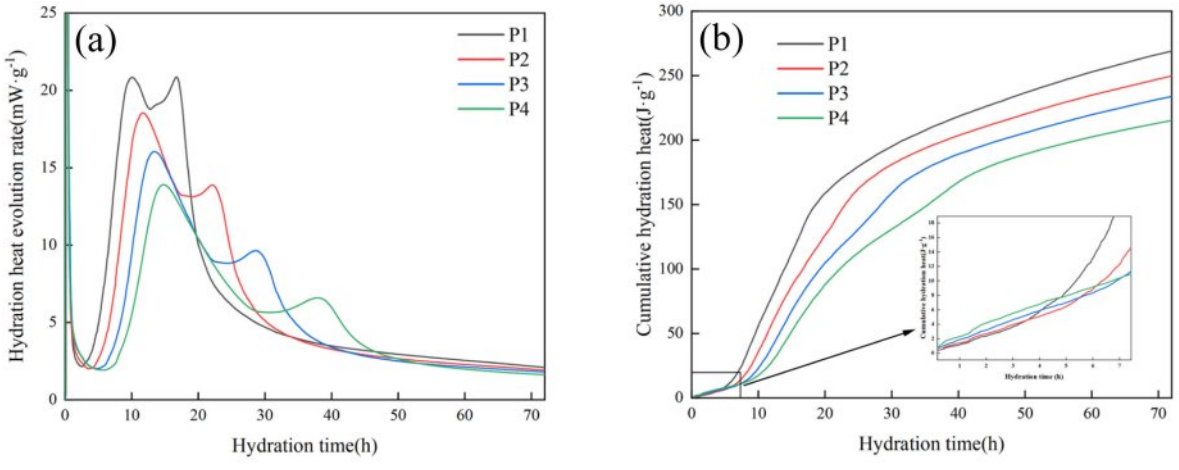

Fig. 11. Hydration heat evolution rate (a) and cumulative hydration heat curves (b) of paste samples for 72 h.

secondary hydration.

In Fig. 11(b), the cumulative hydration heat in the dissolution stage increases with the increase of LS replacement, which is due to the finer LS particles incorporated, which are easier to dissolve and release heat. In the first 3 days, the cumulative heat release decreases with increasing LS replacement, which provides ideas for the use of LS in mass concrete.

NMR analysis

The amplitude on the vertical coordinate of the T_2 relaxation curve is proportional to the number of pores, while the horizontal coordinate represents the pore size. Fig. 12(a) shows that the peak relaxation times of P2, P3, and P4 are shifted to the right by 1.19 ms, 2.6 ms, and 1.67 ms, respectively, compared with P1, and the heights of the peaks are also significantly increased; in Fig. 12(b), the peak relaxation times of the four samples are basically the same but the peaks increase with the increase of lithium slag substitution. This indicates that in the early stage, the doping of lithium slag will not only increase the pore size, but also increase the number of pores, which in turn negatively affects the system. This echoes the compressive strength results.

Comparing Fig. 12(a) and Fig. 12(b), it can be seen that the peaks of each group decreased with the prolongation of the curing time. This indicates that the overall pore space of the system is getting smaller, and LS starts to participate in the secondary reaction, continuously generating hydration products to fill the pore space and reduce the pore diameter, making the system more dense.

MIP analysis

The four types of pores in this work are gel pores (I, <10 nm), transition pores (II, 10-100 nm), capillary pores (III, 100-1,000 nm) and air-pores or fissures (IV, >1,000 nm) [44].

Fig. 13(a) shows the results of MIP experiments of different LSCCM samples at 28d. It can be seen that the doping of LS is still mainly dominated by transition pores and this does not alter the system's most likely

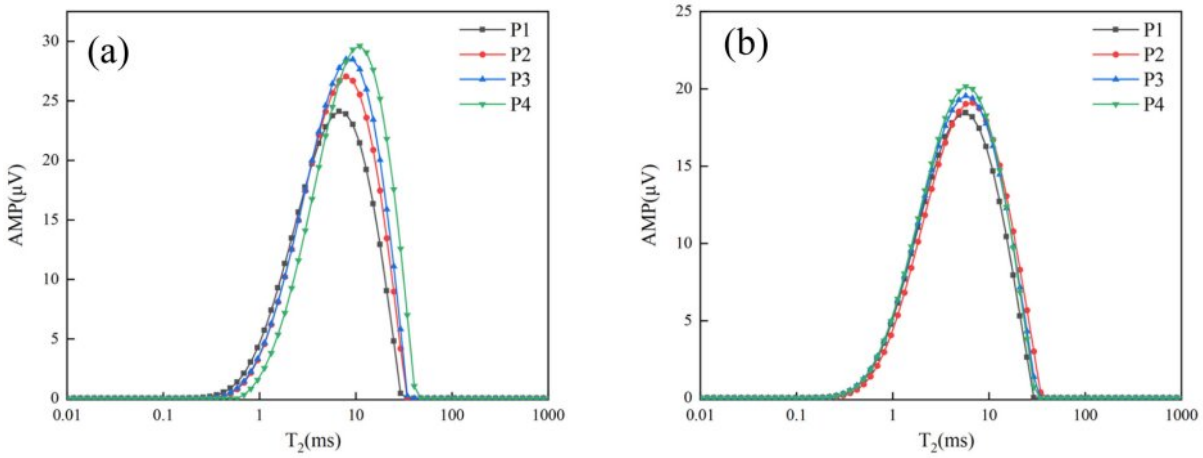

Fig. 12. T_2 relaxation curves: (a) 3d; (b) 28d.

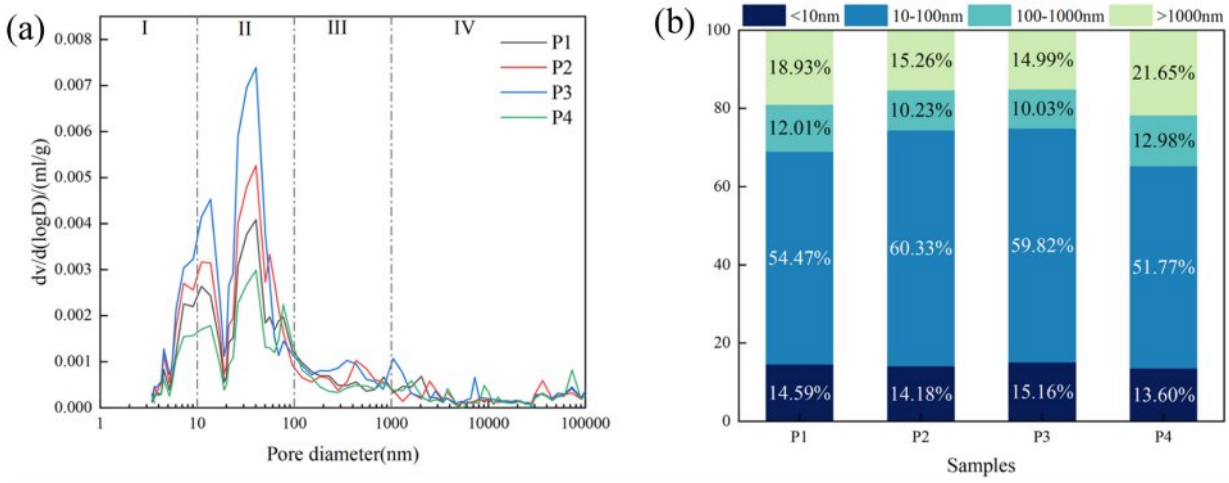

Fig. 13. Pore size distributions (a) and Aperture gradation (b) of LSCCM for 28d.

Table 3. Pearson correlation coefficient.

Pore	Pearson correlation coefficient (r)
gel pores	+0.89
transition pores	+0.89
capillary pores	-0.92
air-pores or fissures	-0.94

pore size. Fig. 13(b) shows the pore occupancy plots of different LSCCM samples. P2 and P3 show a decrease of 19.4% and 20.8% in the number of pores or fissures, respectively, compared to P1, while P4 shows an increase of 14.4% compared to P1. This indicates that the moderate amount of LS will reduce the harmful pores of the system and thus increase the strength of the system. When the LS is in excess, it negatively affects the system.

In this paper, the correlation between pore type and compressive strength is evaluated by calculating the Pearson correlation coefficient. The results are shown in the Table 3. In this paper, the correlation between pore type and compressive strength is evaluated by calculating the Pearson correlation coefficient. The results are shown in the table below. It can be found that the higher the proportion of pores or fissures, the lower the compressive strength. The higher the proportion of gel pores and transition pores, the higher the compressive strength may be. This is also consistent with the compressive strength results.

Conclusion

LS replacing part of cement decreases the fluidity of the system and shortens the setting time.

At 3d and 7d, as the amount of LS replacement cement increases, the compressive strength falls; at 28d, when the amount of LS replacement is 10% and 20%, it enhances the strength of the sample, and when the amount of replacement is 30%, it will have a negative impact on the strength. The strength is best when the LS replacement is 20%, up to 50.2 MPa, which is 9.4% higher than for the pure cement mortar sample.

In the early stage, after mixing LS, basically pozzolanic reaction occurs, but only plays a filling role. In the later stage, C-S-H gel is created when LS combines with the hydration product $Ca(OH)_2$ through a pozzolanic reaction.

The system's overall pore size distribution changes when LS is added. In the early stage, LS only plays the role of filling, while in the later stage, the active ingredients in LS participate in the reaction, and the large pores in the system are continuously filled by the hydration products, resulting in a reduction of the pore size.

References

1. S.A. Rahman, F.U.A. Shaikh, and P.K. Sarker, Constr. Build. Mater. 328 (2022) 123053.
2. D.Y. Hwang and S.H. Lee, J. Ceram. Process. Res. 22[6] (2021) 615-619.
3. C.Y. Kang and S.H. Lee, J. Ceram. Process. Res. 23[2] (2022) 109-112.
4. Y.S. Zhao, X.T. Yue, Y.H. Tang, X.L. An, and X.P. Shang, J. Ceram. Process. Res. 25[5] (2024) 862-870.
5. K. Yuvaraj, M. Sakthival, M. Dhivakar, T. Pradeep, M. Veerapathran, and S. Gowtham, J. Ceram. Process. Res. 25[2] (2024) 254-260.
6. Y.E. Milian, S. Ushak, L.F. Cabeza, and M. Grageda, Sol. Energ. Mat. Sol. C. 208 (2020) 110344.
7. B.L. Li, R.L. Cao, N.Q. You, C. Chen, and Y.M. Zhang, Constr. Build. Mater. 220 (2019) 596-606.
8. V. Rahhal and R. Talero, J. Therm. Anal. Calorim. 78 (2004) 191-205.
9. S. Anandaraj, A.R. Krishnaraja, P. Kulanthaivel, and P.C. Murugan, J. Ceram. Process. Res. 25[1] (2024) 41-47.
10. Xiafei Li, Junzong Feng, Guozhu Zhao, and Xingyu Wu, J. Ceram. Process. Res. 24[5] (2023) 816-826.
11. C. Sailaja, K.T. Thilagham, K.T. Anand, P. Ganeshan, S. Kannan, A.H. Seikh, and A. Ghosh, J. Ceram. Process. Res. 24[4] (2023) 617-625.
12. S. Janani, G.S. Rampradheep, P. Kulanthaivel, and P.C. Murugan, J. Ceram. Process. Res. 23[6] (2022) 884-891.
13. W.B. Gao, S.W. Jian, X. Li, H.B. Tan, B.D. Li, Y. Lv, and J. Huang, J. Clean. Prod. 348 (2022) 131361.
14. Q. Luo, Y.S. Wang, S.X. Hong, F. Xing, and B.Q. Dong, Constr. Build. Mater. 273 (2021) 121723.
15. N.C. Consoli, R.B. Saldanha, L.E.C. Mallmann, T.M.D. Paula, and B.Z. Hoch, Constr. Build. Mater. 157 (2017) 65-74.
16. D.S. Hou, J.L. Zhang, W. Pan, Y. Zhang, and Z.H. Zhang, J. Ducl. Mater. 528 (2020) 151841.
17. Z. Liu, J.X. Wang, Q.K. Jiang, G.D. Cheng, L. Li, Y.X. Kang, and D.M. Wang, J. Clean. Prod. 225 (2019) 1184-1193.
18. GB/T 2419-2005, (2005).
19. GB/T 1346-2011, (2011).
20. GB/T 17671-2021, (2021).
21. M. Yang, C.M. Neubauer, and H.M. Jennings, Cement. Concrete. Res. 5[1] (1997) 1-7.
22. F.J. Robert, Cement. Concrete. Res. 34[3] (2004) 399-408.
23. R.J. Flatt, Mater. Struct. 37 (2004) 289-300.
24. U. Hiroshi, O. Kenji, and U. Shunichiro, Cement. Concrete. Res. 15[4] (1985) 561-572.
25. J.T. Fulvio and M.G. Ellis, Adv. Cem. Res. 1 (1998) 67-74.
26. Y.H. Zhang, Y.L. Wang, T.B. Li, Z.L. Xiong, and Y.P. Sun, Constr. Build. Mater. 161 (2018) 374-380.
27. X.J. Li and J.Y. Hao, Constr. Build. Mater. 181 (2018) 42-48.
28. H.B. Tan, X. Zhang, X.Y. He, Y.L. Guo, X.F. Deng, Y. Su, J. Yang, and Y.B. Wang, J. Clean. Prod. 205 (2018) 536-551.
29. M. Balapour, A. Joshaghani, and F. Althoey, Constr. Build. Mater. 181 (2018) 27-41.
30. L. Lang, N. Liu, and B. Chen, Constr. Build. Mater. 230 (2020) 116971.
31. E. John, T. Matschei, and D. Stephan, Cement. Concrete.

Res. 113 (2018) 74-85.
32. M. Horgnies, L. Fei, R. Arroyo, J.J. Chen, and E.M. Gartner, Cement. Concrete. Res. 89 (2016) 145-157.
33. G. Anbalagan, S. Mukundakumari, K.S. Murugesan, and S. Gunasekaran, Vib. Spectrosc. 50[2] (2009) 226-230.
34. M.S. Li, H. Liu, P. Duan, S.Q. Ruan, Z.H. Zhang, and W. Ge, Constr. Build. Mater. 299 (2021) 123950.
35. N. Li, N. Farzadnia, and S.J. Shi, Cement. Concrete. Res. 100 (2017) 214-226.
36. G.W. Sun, J.J. Zhang, and N. Yan, Constr. Build. Mater. 251 (2020) 118978.
37. M. Nedeljkovic, B. Savija, Y. Zuo, M. Lukovic, and G. Ye, Constr. Build. Mater. 161 (2018) 687-704.
38. H. Zhang, X. Lin, P. Feng, L. Li, and W.B. Wang, Thermochimica Acta. 68 (2019) 178403.
39. B.S. Gebregziabiher, R. Thomas, and S. Peethamparan, Cement. Concrete. Comp. 55 (2015) 91-102.
40. H. Minard, S. Garrault, L. Regnaud, and A. Nonat, Cement. Concrete. Res. 37[10] (2007) 1418-1426.
41. S. Pourche, L. Regnaud, J.P. Perez, and A. Nonat, Cement. Concrete. Res. 39[11] (2009) 989-996.
42. R. Ylmen, L. Wadso, and I. Panas, Cement. Concrete. Res. 40[10] (2010) 1541-1546.
43. L.S. Karen, J. Patrick, and J.M.M. Paulo, Cement. Concrete. Res. 78 (2015) 38-56.
44. X.H. Zeng, X.L. Lan, H.S. Zhu, G.C. Long, and Y.J. Xie, Cement. Concrete. Comp. 122 (2021) 104139.